Composition and the thermoelectric performance of β-Zn_4Sb_3

Eric S. Toberer,[a] Protima Rauwel,[b] Sylvain Gariel,[a] J. Taftø[b] and G. Jeffrey Snyder*[a]

Received 25th June 2010, Accepted 5th August 2010
DOI: 10.1039/c0jm02011g

β-Zn_4Sb_3 is a promising thermoelectric material due to the abundance of zinc and antimony and reports of high efficiency in bulk samples. This work establishes the high temperature properties of β-Zn_4Sb_3 across the phase stability window. By controlling the stoichiometry, the Hall carrier concentration can be tuned from 6–9 $\times$ 10^{19} cm^{-3} without requiring extrinsic dopants. The trend in Seebeck coefficient on carrier concentration is rationalized with a single, parabolic band model. Extremely low lattice thermal conductivity (0.4–0.6 W m^{-1} K^{-1}) coupled with a moderate effective mass (1.2 m_e) and mobility leads to a large figure of merit (zT of 0.8 by 550 K). The single parabolic band model is used to obtain the carrier concentration dependence of the figure of merit and an optimum carrier concentration near 5 $\times$ 10^{19} cm^{-3} is predicted.

A. Introduction

Thermoelectric power generation, which converts the flow of heat into electrical power, could increase our energy efficiency through waste heat capture and co-generation. The potential for improved automotive fuel efficiency through exhaust waste heat capture is particularly attractive. However, significant *material* improvements are required for thermoelectric power generation to become widespread.

The efficiency of a thermoelectric generator is governed by the Carnot efficiency ($\Delta T/T_{hot}$) and a material-specific component, governed by the figure of merit (zT). Eqn (1) reveals that a large figure of merit is achieved with the optimization of conflicting properties – namely large Seebeck coefficient (α), small electrical resistivity (ρ) and small thermal conductivity (κ).[1–6] All of these properties depend heavily on the carrier concentration and typical thermoelectric materials are semiconductors with optimum doping levels of 10^{19}–10^{21} carriers cm^{-3}.

$$zT = \alpha^2 T/\rho\kappa \quad (1)$$

Commercially, the thermoelectric market is dominated by Bi_2Te_3 and PbTe-based materials with peak zT values near 1. Concerns over the toxicity and cost of the commercial materials are encouraging the transition to alternative materials if high zT can be reproducibly obtained and lifetime stability can be demonstrated. In the moderate temperature range (400–600 K), the primary alternatives to the tellurides are β-Zn_4Sb_3, the half-Heuslers, and $Mg_2Si_{1-x}Sn_x$.[7,8]

The room temperature structure of β-Zn_4Sb_3 ($R\bar{3}c$) contains an anionic framework composed of 30 Sb, divided between 6 Sb_2^{4-} dimers and 18 isolated Sb^{3-}.[9,10] A charge balanced composition thus requires 39 Zn^{2+}, yielding a charge balanced composition at $Zn_{3.9}Sb_3$. Of these Zn atoms, 36 are on framework sites and the remaining 3 are distributed among three crystallographically unique interstitial sites.[9] The Sb dimers exhibit Einstein modes, suggesting a shallow potential along the c-axis.[11] Evidence of super-ionic transport of Zn within β-Zn_4Sb_3 likewise suggests rather shallow potentials for the Zn species.[12] This disordered structure, depicted in Fig. 1, is stable from 250–673 K.[13] A multitude of synthetic routes have been employed to produce β-Zn_4Sb_3, including quenching from the melt,[7,14,15] mechanical alloying of the elements,[13] flux-growth,[16] zone melting,[17] reactive hot-pressing,[18] sinter-forging[19] and gradient freeze methods.[9,20,21]

High resolution diffraction work yielded a stoichiometry of $Zn_{3.83}Sb_3$, rather than the charge balanced $Zn_{3.9}Sb_3$.[9,16] Such a composition is Zn deficient, consistent with the p-type semiconductor behavior observed in all samples to date.[7] No samples have been prepared with transport behavior characteristic of an intrinsic semiconductor. This may indicate the charge balanced composition $Zn_{3.9}Sb_3$ is not stable at room temperature. The width of the β-Zn_4Sb_3 phase has been estimated as 0.2 at. % Zn[21] and 0.5 at. % Zn.[13] Analysis of the low temperature phase transitions has been viewed in light of this small composition window.[16] The exact values for phase stability should be approached with some caution, as the microprobe spacial resolution is insufficient to observe nanoparticle inclusions. Indeed, we have found β-Zn_4Sb_3 at a 4Zn:3Sb composition yields Zn

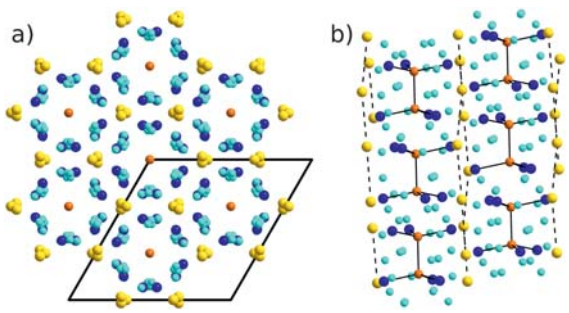

Fig. 1 Structure of β-Zn_4Sb_3 along the rhombohedral (a) [001] and (b) [110] directions. Sb_2^{4-} dimers (orange) are capped by Zn^{2+} atoms (blue). Isolated Sb^{3-} (yellow) form columns along [001], denoted by the dashed lines. Interstitial Zn^{2+} atoms (teal) are found at three crystallographically unique sites with low occupancy ($\sim$ 5%).

[a]*Materials Science, California Institute of Technology, 1200 E. California Blvd., Pasadena, California, 91125, USA. E-mail: jsnyder@caltech.edu*
[b]*Department of Physics, University of Oslo, P.O. Box 1048, Blindern, N-0316, Oslo, Norway*

nanoparticle inclusions which are only observable by transmission electron microscopy.[22] This nanoparticle formation suggests a decreasing Zn solubility on cooling, leading to diffusion-limited precipitation.

Despite the great potential for β-Zn_4Sb_3, systematic studies of the electronic properties as a function of composition or carrier concentration are absent. Likewise, analysis of the electronic properties of β-Zn_4Sb_3 with extrinsic dopants[14–16,23–26] or as a composite[27] (or both) has been missing a fundamental understanding of the parent phase. This work investigates β-Zn_4Sb_3 across the available phase stability range as well as the bounding biphasic compositions. Measurement of the high temperature transport properties are reported for polycrystalline samples within the β-Zn_4Sb_3 composition window.

B. Experimental

Samples with composition near the β-Zn_4Sb_3 phase (56–58 at. % Zn) were prepared by direct reaction of the elements in fused-silica ampoules sealed under vacuum (10^{-5} torr). The reactants were melted by heating at 1073 K for 8 h, followed by quenching in water. To provide homogeneous fine grain powders for sintering, mechanical alloying was performed under argon in a SPEX Mixer/Miller 8000 series mill for a total of 3 h. Hot pressing of the resulting powder was performed under argon at 623 K for 1 h followed by a 2 h stress-free anneal at 573 K.

Following hot pressing, the resulting ingots were sliced and characterized for composition and microstructure through a combination of X-ray diffraction (XRD), scanning electron microscopy (SEM) and transmission electron microscopy (TEM). Powder XRD patterns were measured on a Philips XPERT MPD diffractometer with a copper source operated at 45 kV and 40 mA and subject to Rietveld refinement using the X'Pert Plus package. Fits yielded R_p values of 7–8, without refining the occupancy or positions of the interstitial model.

Scanning electron microscopy was performed on a LEO 1550 VP Scanning Electron Microscope (SEM) and electron probe microanalysis (EPMA) utilized a JEOL JXA-8200. Conventional and high resolution TEM were performed with a JEOL 2010F operating at 200 kV. Samples were first prepared by crushing and dispersing them in ethanol. A drop of this suspension was placed on a holey carbon grid. Another set of samples were prepared by mechanical thinning and ion milling.

Transport measurements to 550 K were then initiated, with care taken to ensure neither the carrier concentration nor room temperature Seebeck coefficient changed between runs (variation less than 5×10^{18} cm^{-3} and 3 μV K^{-1}). As discussed above, the volatility of Zn makes transport measurements to high temperatures difficult. Measurements at temperatures above 600 K often showed irreversible behavior. Electrical resistivity was determined using the van der Pauw technique and the Hall coefficient was measured with a 2 T field. The Seebeck coefficient was measured with a constant 10 K temperature gradient across the sample and Chromel-Nb thermocouples. A Netzsch LFA 457 was used to measure thermal diffusivity and the heat capacity was measured with a Perkin Elmer Diamond DSC.

C. Results and discussion

Composition and microstructure

The synthesis of β-Zn_4Sb_3 (56–58 at. % Zn) resulted in dense ingots (> 98% theoretical density) which were characterized for phase purity and composition with a combination of powder X-ray diffraction (XRD) and electron microscopy. Fig. 2a shows the powder pattern and Rietveld refinement profile for a phase pure sample of β-Zn_4Sb_3 utilizing the interstitial model.[9] For compositions outside of the stable composition window, secondary phases of either Zn or ZnSb were observed by XRD, as expected from the binary phase diagram. Quantitative phase analysis was used to estimate the molar fraction of these secondary phases. For the composition range investigated, as much as 18 vol. fraction ZnSb and 2 vol % Zn were observed. This difference in phase ratio simply arises from application of the Lever rule. For elemental Zn, the accuracy of these estimates is compromised due to significant peak overlap with the dominant β-Zn_4Sb_3 phase and volume fractions less than $\sim$ 1% are not statistically significant.

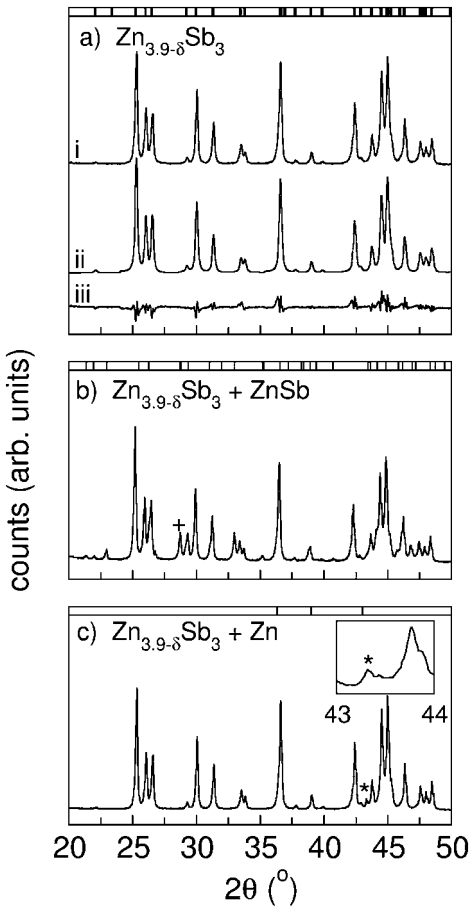

Fig. 2 a) Powder X-ray diffraction pattern (i) of representative, single phase β-Zn_4Sb_3 sample. Rietveld refinement (ii) and difference profile (iii) are shown in the lower curves. Peak positions for β-Zn_4Sb_3 are shown along the top border. b) Powder XRD pattern from a composite of β-Zn_4Sb_3 and ZnSb (ZnSb peak positions noted along top edge). c) Similarly, pattern from a β-Zn_4Sb_3 and Zn composite sample with Zn peak positions along top edge. The two dominant Zn peaks overlap with those of β-Zn_4Sb_3, the third peak is shown in the inset.

Fig. 3 shows the relationship between the synthetic composition and the average microprobe composition (average of five 40 μm × 200 μm regions). The scatter of these measurement was <0.2 at. %, however microprobe measurements can be subject to systematic errors on the order of 0.5 at. %. This sampling size was selected to include a statistically significant number of grains and grain boundaries. Good agreement is found until high Zn compositions, where a decrease in Zn content from the synthetic composition is observed. Zn loss could arise from volatility during the pressing or due to adhesion of metallic Zn to the vial walls. This second effect was clearly seen in efforts to prepare samples with higher Zn content (> 58 at. % Zn). Given the extensive crystallography work which suggests a β-Zn_4Sb_3 stoichiometry of ~ 56.1 at. % Zn, and the *p*-type nature of the material (recall a charge balanced $Zn_{3.9}Sb_3$ corresponds to 56.5 at. % Zn), we are surprised that the microprobe results give such a high Zn content for single phase materials (57.0–57.2 at. % Zn). At this juncture, such a shift is attributed to systematic errors in these microprobe measurements. Transmission electron microscopy studies, discussed below, do not find Zn nanoparticles in samples of this 'single phase' composition range. Separately, we have observed composition fluctuations in the material at submicron length scales *via* atom probe tomography.[28]

Fig. 4 shows that the molar fractions of Zn and ZnSb observed *via* powder XRD were consistent with the quantities expected from microprobe measurement (dashed lines Fig. 4). The single phase region of β-Zn_4Sb_3, as observed by XRD, is found to be ~ 0.2 at. % Zn wide from these microprobe measurements (Fig. 3). This phase width is consistent with prior electron-probe micro analysis work.[21]

We have previously investigated β-Zn_4Sb_3 at a 4Zn:3Sb composition and found embedded Zn nanoparticles in the β-phase matrix *via* transmission electron microscopy (TEM).[22] In the present work, samples across a broad stoichiometry range were investigated by TEM following hot-pressing. For samples which appeared to be entirely β-Zn_4Sb_3 by powder XRD, TEM found virtually no evidence of secondary phases. However, extremely bright spots could be observed which appear to correspond to voids ~ 8 nm in diameter within the grains (Fig. 5a). Additonal voids at the grain boundaries were observed which were significantly larger on average (~ 20 nm). Fig. 5b shows histograms for these voids. High resolution images of these voids (not shown here) show that they are faceted and near

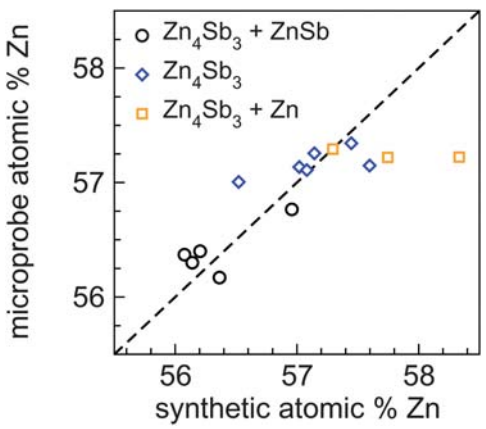

Fig. 3 Good agreement in stoichiometry was found between nominal synthetic compositions and microprobe analysis of the prepared ingots. At high Zn concentrations, some loss of Zn during synthesis resulted in an upper limit to the Zn content of ~ 57.2%. X-ray diffraction of the resulting ingots yielded single phase β-Zn_4Sb_3, as well as composites with either ZnSb or elemental Zn, as denoted respectively with circles and squares.

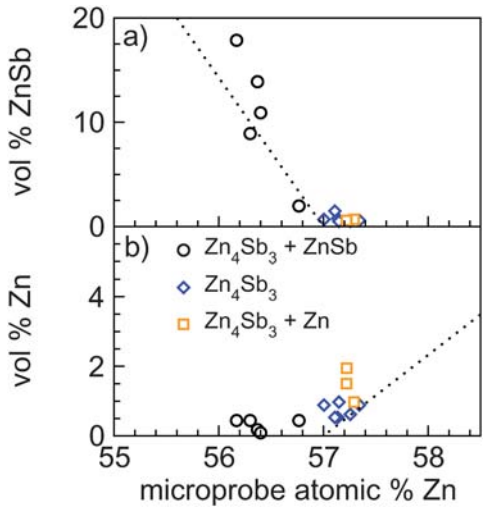

Fig. 4 Rietveld analysis using three phases (β-Zn_4Sb_3, ZnSb, and elemental Zn) yielded β-Zn_4Sb_3 as the dominant phase for all samples. Volume fraction of (a) ZnSb and (b) Zn as s econdary phases are shown for all samples. Volume fractions below 1% are believed to be artifacts of the fitting procedure. The dotted line in each panel leads to the end member ZnSb and Zn, respectively.

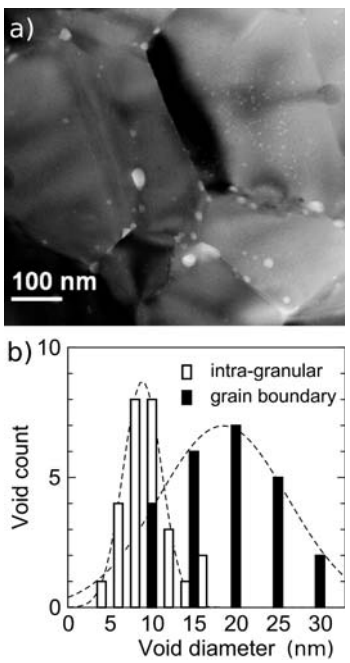

Fig. 5 (a) TEM micrograph showing several β-Zn_4Sb_3 grains with voids at the grain boundary and embedded within the grains. (b) Histogram for the average void diameter using for the grain boundary and embedded voids using histogram bin sizes of 2 and 5 nm, respectively.

hexagonal. The cause of these voids remains unresolved; presumably, they formed due to the extrusion and subsequent reincorporation or loss of a secondary phase. The high temperature phase diagram near β-Zn_4Sb_3 has a number of phase transformations which could be implicated in such behavior. Fig. 5a reveals that the density of these voids is quite high, the implications of this for thermal transport will be discussed below. Similarly porous microstructure was observed for Zn-rich samples. As the elemental Zn content was limited synthetically, as discussed above, Zn nanoparticles were not commonly observed. For Sb-rich samples where XRD could identify ZnSb as a secondary phase, ZnSb nanoparticles with diameters of $\sim$ 10 nm were observed (Fig. 6). The formation and high temperature transport properties of these nanoparticle-rich materials will be described in a separate report.

High resolution TEM of the pure β-Zn_4Sb_3 phase (after hot pressing) was also conducted; Fig. 7a shows a grain oriented along the <001> axis taken with a defocus (Δf) = -60 nm. At this defocus, the atomic potentials of the Sb atomic columns are represented as bright spots. At other defoci for this particular thin foil thickness, the atomic arrangements were more difficult to interpret. After simulations using the multislice calculations incorporated in the JEMS (Java Electron Microscope Software) simulation package, shown as the background image in Fig. 7b, the thin foil thickness was estimated to be around 105 nm. In the upper left inset of Fig. 7b, the projected crystal potential is shown along the <001> axis. When the electron beam passes through a crystal, its kinetic energy is perturbed by the atomic potentials. The phase shift induced is represented by the projected crystal potential. One observes that the distances between the Zn^{2+} atoms and the distances between Sb^{3-} atoms are resolved. The projected crystal potential is created without taking into account the optics of the TEM. The lower left inset in Fig. 7b is the positions of the atomic columns (Sb (blue) and Zn (red)) on the simulated HR image. All simulations were performed using the interstitial Zn model. At this defocus and foil thickness, the Sb_2^{4-} dimer columns have brighter spots compared to the non-bonding Sb^{3-} and Zn^{2+} atoms. The point to point resolution of the microscope is 1.9 Å and is therefore unable to resolve the atomic spacing between the Sb^{3-} group of atoms along the <001> directions. The potentials of these groups of atoms are therefore represented as individual bright spots in the HR image, while the Zn^{2+} are not visible for these imaging conditions.

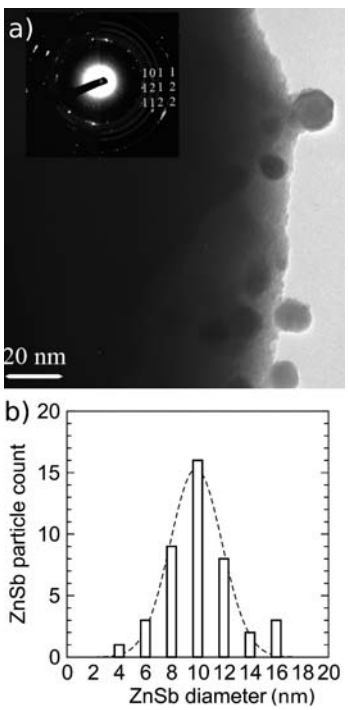

Fig. 6 (a) For Zn-deficient compositions of β-Zn_4Sb_3, ZnSb nanoparticles are observed by TEM. The inset is a selected area diffraction pattern of the ZnSb nanoparticles with reflections corresponding to the orthorhomic ZnSb structure. (b) The ZnSb particles have an average diameter of 10 nm and a narrow size distribution.

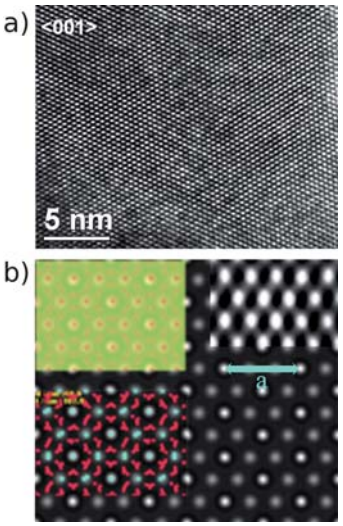

Fig. 7 (a) HRTEM micrograph of β-Zn_4Sb_3 taken along the <001> zone axis. (b) The projected potential is shown in the upper left inset, while the atomic arrangement is shown in the lower left inset. The background image shows the simulated HRTEM image along <001>. The brightest points are clearly the Sb dimers, while the lighter points correspond to the isolated Sb. As in the experimental image, Zn is not observed under these imaging conditions. The upper right inset is the micrograph from (a) after re-scaling.

Transport in β-Zn_4Sb_3

The first in-depth investigation of β-Zn_4Sb_3 reported essentially line compound behavior with the carrier concentration fixed at 9×10^{19} cm^{-3}.[7] However, subsequent investigations reported a broad range of transport properties. The first question we sought to address was: What are the transport properties of phase-pure β-Zn_4Sb_3 and how do they vary with stoichiometry? Hall coefficient measurements found that holes are the majority carriers for all compositions studied ($n_H = 1/R_He$). Carrier concentrations were obtained between 6–9 $\times$ 10^{19} cm^{-3}, and efforts to extend this range resulted in the formation of either Zn or ZnSb. Simple charge counting from the Hall carrier concentration range would suggest the the room temperature phase width of β-Zn_4Sb_3 is 0.02 atomic % Zn. However, density functional theory calculations suggest that the Fermi surface near the valence band edge is quite complex (both *n*- and *p*-type character), and the measured Hall coefficient corresponds to

a valence imbalance that is much less (a factor of two) than the actual valence imbalance.[29] This narrow range (< 0.1 atomic % Zn) reveals why few samples in the literature are single phase. Indeed, obtaining phase-pure samples in this study was an empirical process which iteratively adjusted the stoichiometry to account for Zn loss.

With this understanding of the phase stability range, we can investigate how the transport properties vary with composition. Fig. 8 shows the carrier concentration at 300 K and the corresponding Seebeck coefficient for both single phase and composite samples. As generally expected, increasing carrier concentration in the single phase regime leads to a decrease in the Seebeck coefficient. The transport behavior of pure β-Zn_4Sb_3 can be modeled with a single parabolic band approximation with transport limited by acoustic phonon scattering ($\lambda = 0$). This final assumption is supported below from the temperature dependence of the mobility. An effective mass (m^*) of $1.23m_e$ is found to describe the single-phase transport data well. Generating this curve involves solving eqn (2) and 4 for various chemical potentials (η). Here, ζ is the reduced carrier energy and $f_o(\eta)$ is the Fermi distribution function. As discussed above, the complex Fermi surface may introduce inaccuracies into this calculation, and the magnitude of the m^* obtained is simply an approximation. Also shown in Fig. 8 are composite samples which contained either ZnSb or Zn secondary phases. At the limit of low secondary phase doping, the behavior is similar to the matrix phase. The inclusion of a small amount of metallic Zn suggests from the phase diagram that the matrix of β-Zn_4Sb_3 is at the highest allowable Zn composition and thus the lowest carrier concentration. Similarly, the dilute presence ZnSb suggests the β-Zn_4Sb_3 should be Zn deficient and have the highest carrier concentration attainable. With increasing fraction of secondary phase, an effective medium in properties is obtained. This is clearly seen in the inset of Fig. 8, where phase pure ZnSb[27] is at the extension of the line generated by the composite of ZnSb/β-Zn_4Sb_3.

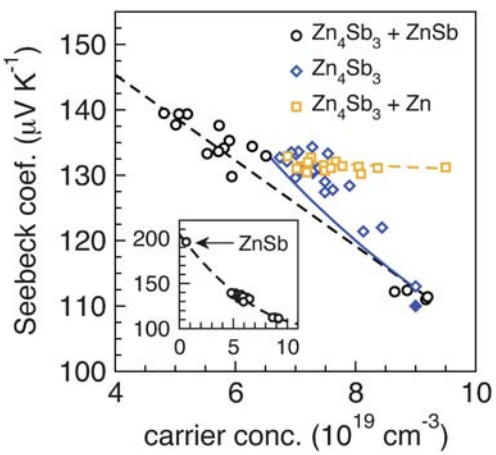

Fig. 8 Room temperature Hall carrier concentration and Seebeck coefficient for samples with synthetic composition 56–58 atomic % Zn. The open diamonds show single phase β-Zn_4Sb_3 samples from this study while the filled diamond shows the value reported in Ref. 7. The solid purple curve shows β-Zn_4Sb_3 is well described by a single parabolic band with an effective mass of 1.23 m_e within the carrier concentration range accessible. Also shown are the results outside of the single phase window (Zn or ZnSb inclusions) and guides to the eye describing this behavior. The inset includes data from Ref. 27 for pure ZnSb.

$$\alpha = \frac{k}{e}\left(\frac{(2+\lambda)F_{1+\lambda}(\eta)}{(1+\lambda)F_{\lambda}(\eta)} - \eta\right) \quad (2)$$

$$F_r(\eta) = \int_0^{\infty} \zeta^r f_o(\eta) d\zeta \quad (3)$$

$$n = \frac{4}{\sqrt{\pi}}\left(\frac{2\pi m^* kT}{h^2}\right)^{3/2} F_{1/2}(\eta) \quad (4)$$

The carrier concentration dependence of μ can be predicted using eqn (4) and 5 within the approximation of a single parabolic band. Here, μ_o is a free parameter related to the intrinsic mobility. Fig. 9 shows that the mobility exhibits a strong dependence on carrier concentration, beyond that expected for a single parabolic band and transport limited by acoustic phonon scattering. Many factors could account for this deviation in mobility, including carrier scattering from interstitial Zn, variation in microstructure (*e.g.* void concentration), or non-parabolic band features.[29] This inverse relationship between mobility and carrier concentration yields extremely similar resistivity magnitudes across the samples investigated (Fig. 11).

$$\mu_H = \frac{\mu_o \pi^{1/2} F_{\lambda}(\eta)}{2\Gamma(1+\lambda)F_{1/2}(\eta)} \quad (5)$$

High temperature electrical transport

For all single phase samples, an increase in Hall carrier concentration with increasing temperature is observed within the measurement range (Fig. 10a). Prior investigation of the β-phase found a peak in the Seebeck coefficent at $\sim 180\ \mu V\ K^{-1}$ at 623 K, suggesting a thermal band gap of ~ 0.23 eV ($E_g = 2e\alpha_{max}T_{max}$).[30,31] Such a small band gap, leading to minority carrier activation, may be implicated in this high temperature behavior. With increasing

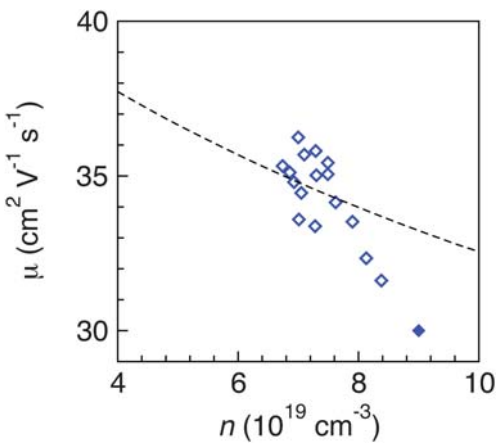

Fig. 9 Room temperature Hall mobility shows a dependence on the carrier concentration close to that expected from classical transport equations with the assumption mobility limited by acoustic phonon scattering (dashed line). The solid point shows the value reported in Ref. 7.

temperature, the Hall mobility decays (Fig. 10b) rapidly. This decay fits well to a power-law with a coefficient of ~ 1.2, implicating acoustic phonon scattering as the source of the reduced mobility with increasing temperature. The decay in mobility leads to the observed increase in electrical resistivity with increasing temperature (Fig. 11). The Seebeck coefficient is found to rise with increasing temperature (Fig. 12), with minority carrier activation leading to the deviation from linear behaviour at high temperature.

Thermal transport

Heat capacity measurements of phase pure β-Zn_4Sb_3 are shown in Fig. 13, along with the Dulong-Petit value. Low temperature data is reproduced from Ref. 32 and shows the α to β transition at ~ 250 K. The heat capacity at room temperature is above the Dulong-Petit value, consistent with a Debye temperature of 250 K.[32] While these heat capacity results are larger near room temperature than those obtained in Ref. 7, similar values are obtained at high temperature.

The thermal conductivity (κ) is the product of the density, heat capacity (C_p), and thermal diffusivity. Thermal diffusivity measurements of single phase polycrystalline disks of β-Zn_4Sb_3 were obtained to determine the thermal conductivity. Fig. 14 shows the total thermal conductivity for samples across the accessible concentration range. To determine the electronic component of the thermal conductivity, the Lorenz number was estimated using eqn (6) with the assumption of transport dominated by acoustic scattering and a single parabolic band. Note that the chemical potential (η) of each sample varies with temperature, leading to the calculation of a Lorenz number at every temperature of interest. With this estimate for κ_e, the lattice component of thermal conductivity (κ_L) can be determined ($\kappa = \kappa_e + \kappa_L$). Fig. 14 shows κ_L is extremely low (0.4–0.6 W m^{-1} K^{-1}) and exhibits a decay with increasing temperature as expected in a crystalline material where κ_L is dominated by phonon-phonon scattering. In comparison, the minimum thermal conductivity calculated using the approach of *Cahill* is quite similar, yielding a value of ~ 0.46 W/mK at 500 K. An additional comparison could be made with the amorphous $Zn_{41}Sb_{59}$, which possessed a lattice thermal conductivity of ~ 0.2 W/mK at 300 K.[33] Comparing these results for lattice thermal conductivity with those previously published by *Caillat*, the high temperature values are quite similar.[7] Near room temperature, however, the lattice thermal conductivity of the samples discussed here are significantly lower (particularly when the differences in employed heat capacity are considered). This difference may arise from scattering of acoustic phonons by the nanoscale voids within the grains (Fig. 5). At high temperature, the increased Umklapp scattering may wash out the scattering effects of these voids.

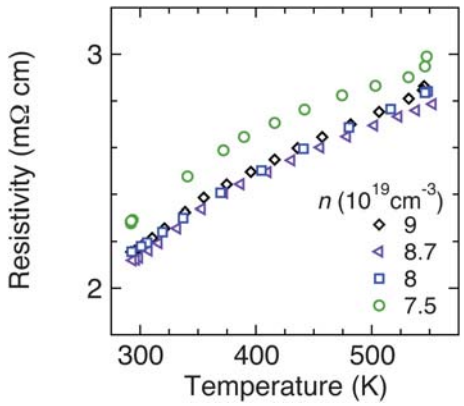

Fig. 11 Resistivity for several β-Zn_4Sb_3 samples, room temperature carrier concentrations given.

$$L = \left(\frac{k}{e}\right)^2 \frac{3F_0(\eta)F_2(\eta) - 4F_1(\eta)^2}{F_0(\eta)^2} \quad (6)$$

Thermoelectric efficiency

The thermoelectric figure of merit (zT) is shown in Fig. 15 from the measurements described above. All single-phase compositions of β-Zn_4Sb_3 are found to be excellent thermoelectric materials, with

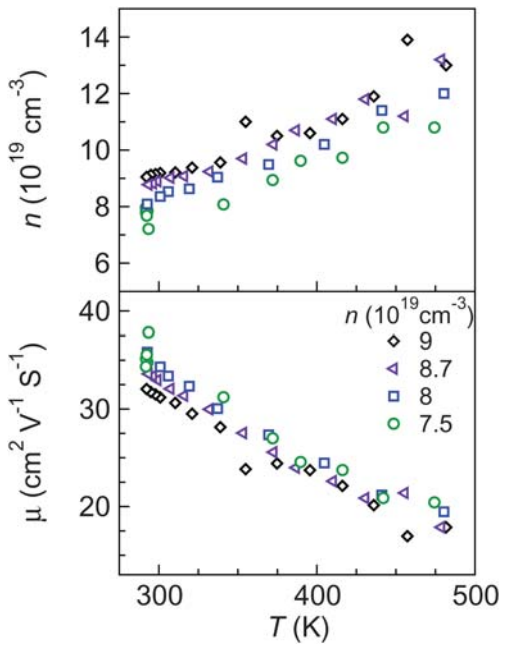

Fig. 10 High temp Hall effect measurements of β-Zn_4Sb_3 are used to calculate the a) carrier concentration b) mobility.

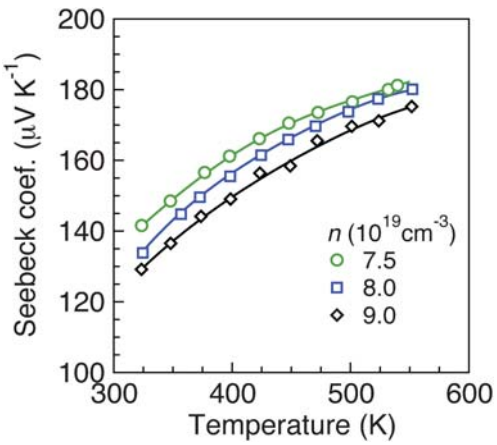

Fig. 12 Seebeck coefficients for several β-Zn_4Sb_3 samples, room temperature carrier concentrations given.

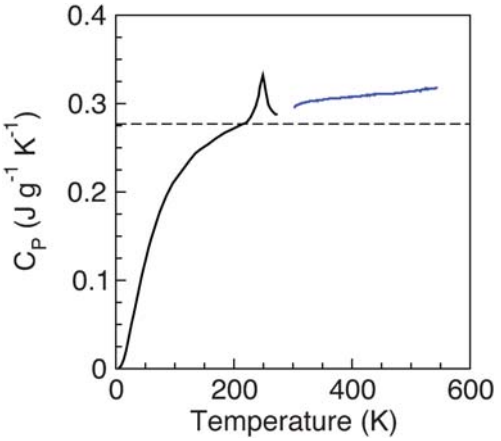

Fig. 13 Low temperature β-Zn_4Sb_3 heat capacity from Ref. 32 and representative high temperature heat capacity from the samples described here. The dashed line shows the Dulong-Petit approximation for the heat capacity. The peak in the heat capacity arises from the α to β phase transition.

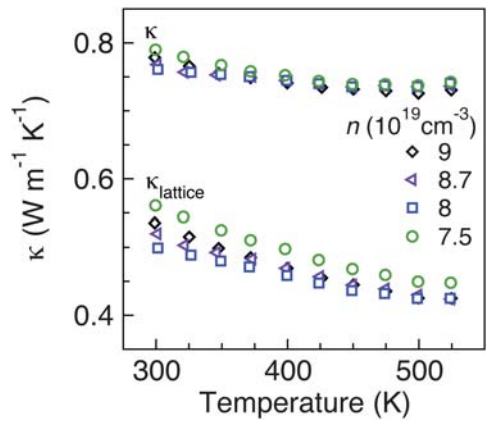

Fig. 14 Thermal conductivity (κ) and lattice thermal conductivity (κ_L) for several β-Zn_4Sb_3 samples, room temperature carrier concentrations given.

zT of 0.8 by 550 K. Increased zT is anticipated at higher temperatures,[7] however signs of sample volatility in the evacuated instruments begin to appear above this temperature. The use of β-Zn_4Sb_3 in power generation applications at higher temperatures will require solutions to suppress this sublimation.

The carrier concentration dependence of zT can be approximated from the experimental data and a single parabolic band model with the assumption of acoustic phonon scattering ($\lambda = 0$) using eqn (7)–(9). Fig. 16 shows that the carrier concentrations accessible with single phase window are close to, but do not include, the peak zT. At higher temperatures, the effect of minority carriers will be more detrimental to zT at lower carrier concentrations, and thus the optimum zT may shift to higher carrier concentrations. Such a prediction would require parameters for a two band model, which has not been established. Note that the high temperature carrier concentration (Fig. 10a) is used for the 500 K calculation.

$$zT = \frac{\alpha^2}{L + (\psi\beta)^{-1}} \tag{7}$$

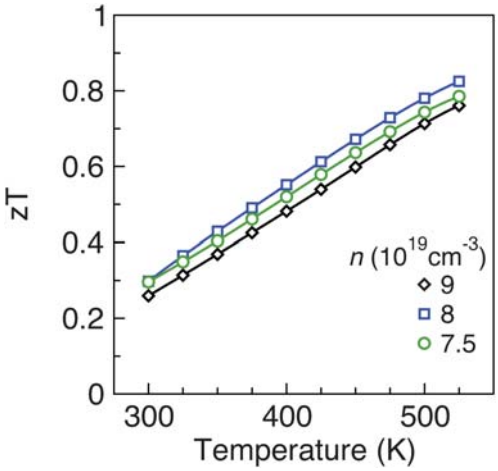

Fig. 15 Thermoelectric figure of merit (zT) obtained for samples across the carrier concentration range given.

$$\beta = \frac{\mu_o (m^*/m_e)^{3/2} T^{5/2}}{\kappa_L} \tag{8}$$

$$\psi = 2e\left(\frac{2\pi k m_e}{h^2}\right)^{3/2} \frac{F_\lambda(\eta)}{\Gamma[1+\lambda]} \tag{9}$$

A material's inherent suitability for thermoelectric performance can be estimated from the the intrinsic mobility (μ_o), effective mass (m^*), and lattice thermal conductivity (κ_L). The quality factor ($\beta = \mu_o m^{*3/2}/\kappa_L$) can be used to estimate a maximum attainable zT, provided the carrier concentration can be appropriately tuned. Considering β-Zn_4Sb_3, the electronic properties ($\mu_o m^{*3/2}$) are inferior to the classic thermoelectric materials such as PbTe, as shown in Table 1. However, the lattice thermal conductivity of β-Zn_4Sb_3 is significantly lower than the commercial tellurides, leading to the excellent thermoelectric performance at 500 K.

The low κ_L arises from scattering sources at multiple length scales which scatter a broad range of phonon frequencies. These sources include: (a) Partially occupied interstitial sites, leading to

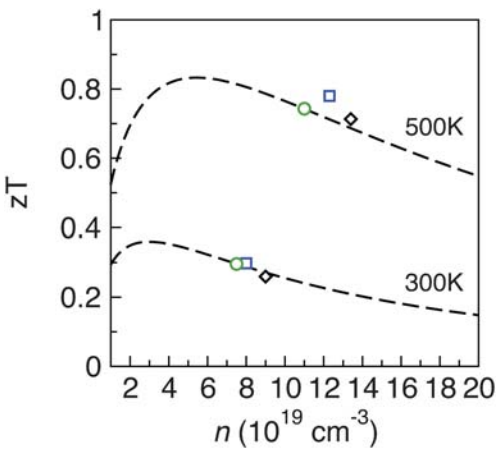

Fig. 16 A single parabolic band model is used to predict zT at 300 and 500 K based on the experimental transport results for β-Zn_4Sb_3.

Table 1 Fundamental transport properties of Zn-Sb based materials and state-of-the-art thermoelectrics at 300 K using the single parabolic band assumption. The glass $Zn_{41}Sb_{59}$ is included for a comparison of the lattice thermal conductivity

	μ [cm²/Vs]	m^* [m_e]	κ_L [W/mK]	β
β-Zn_4Sb_3	35	1.2	0.5	92
ZnSb	100	0.4	2.6	10
$Zn_{41}Sb_{59}$ (am.)[33]	—	—	0.2	—
PbTe	250	0.3	2.0	20
$Ba_8Ga_{16}Ge_{30}$[34]	24	1.8	1.0	58

point defect scattering,[9] (b) Soft, anharmonic bonding, as indicated by the high ionic conductivity and low energies of the various interstitial models.[12,35] (c) 'Nanodomains' of the low temperature ordered structure revealed in the high temperature structure through pair distribution fuction (PDF) analysis.[36] (d) Dumbbell rattling motion of the Sb dimers, leading to Einstein-like modes in the phonon dispersion,[11] (e) Depending on composition, TEM reveals nanovoids or nanoparticles of Zn or ZnSb embedded in the β-Zn_4Sb_3 matrix.[22] We thus find scattering sources at a variety of length scales, ranging from point defects to nanostructures, which can scatter a broad spectrum of phonons. Concurrent with a wide range of scattering sources, much of the available phonon spectrum in β-Zn_4Sb_3 is expected to be low velocity optical modes which arise from the complex cell and the large mass contrast between Zn and Sb.

Improving the electronic properties (optimizing carrier concentration, enhancing $\mu_o m^{*3/2}$) of a thermoelectric material generally involves chemical substitutions or tailored nanostructures. Thus far, work on β-Zn_4Sb_3 has concentrated on alloying control the carrier concentration. A variety of dopants have been investigated (Mg, Cd, Hg, Al, Ga, In, Pb, Sn, Bi, Se).[14–16,23–26] however, most only exhibit a low solubility in the β phase. Alloying with Cd has been shown to increase point defect scattering and lower the lattice thermal conductivity.[20] Carrier concentration control has been investigated with trivalent In substitution of divalent Zn.[14] Difficulties in understanding the results of doped β-Zn_4Sb_3 can stem from the presence of secondary phases (typically Zn and/or ZnSb) which can dramatically effect the electronic properties.

From our understanding of composition and the thermoelectric performance of β-Zn_4Sb_3, several previous conclusions can be re-evaluated. For example, the spatial dependence of the Seebeck coefficient in a β-Zn_4Sb_3 sample grown by the gradient freeze method has been previously investigated with a scanning microprobe system.[37] Seebeck coefficient values were found to range from 100–130 μV/K, and were attributed to differences in crystal orientation. From our investigation, this range may instead reflect variation in stoichiometry across the sample. Likewise, the "β-Zn_4Sb_3" we previously prepared for resonant ultrasound spectroscopy methods which had a room temperature Seebeck coefficient of 160 μV/K likely had a secondary phase of ZnSb.[32] A wide range of thermopower values has been observed in spark plasma sintered (SPS) β-Zn_4Sb_3 and attributed to sample compaction issues in the synthesis.[38] From the present work, this variation may be due to the presence of impurity phases such as Zn and ZnSb. SPS could drive the formation of these phases due to the high volatility of Zn at elevated temperatures and the 'super-ionic' nature of the Zn transport in β-Zn_4Sb_3.[12] While a complete understanding of densification during the SPS processing of an volatile ionic conductor remains elusive, it is conceivable that there is a connection between phase stability and resulting density.

D. Conclusions

In the search for alternatives to telluride-based thermoelectric materials, β-Zn_4Sb_3 is a highly attractive candidate due to the low toxicity and cost of the constituent elements. However, implementation of this material for waste heat recovery requires an complete understanding of the relevant transport properties. To this end, phase-pure β-Zn_4Sb_3 was synthesized across the stable compositional window and the thermoelectric properties were characterized to high temperature. The carrier concentration of β-Zn_4Sb_3 can be controlled simply *via* the stoichiometry and clearly impacts the magnitude of the Seebeck coefficient. High thermoelectric efficiency is obtained above ~ 450 K, due to the extremely low lattice thermal conductivity and near-optimized carrier concentration.

References

1 G. J. Snyder and E. S. Toberer, *Nat. Mater.*, 2008, **7**, 105.
2 S. M. Kauzlarich, S. R. Brown and G. J. Snyder, *Dalton Trans.*, 2007, 2099.
3 G. S. Nolas, J. Poon and M. Kanatzidis, *MRS Bulletin*, 2006, **31**, 199–205.
4 G. Chen, M. S. Dresselhaus, G. Dresselhaus, J.-P. Fleurial and T. Caillat, *Int. Mater. Rev.*, 2003, **48**, 45–66.
5 C. Wood, *Rep. Prog. Phys.*, 1988, **51**, 459–539.
6 D. and M.G., *Solid State Phys.*, 1997, **51**, 81–157.
7 T. Caillat, J.-P. Fleurial and A. Borshchevsky, *J. Phys. Chem. Solids*, 1997, **58**, 1119–1125.
8 Zaitsev, *Phys. Rev. B: Condens. Matter Mater. Phys.*, 2006, **74**, 045207.
9 G. Snyder, M. Christensen, E. Nishibori, T. Caillat and B. Iversen, *Nat. Mater.*, 2004, **3**, 458–463.
10 G. A. Papoian and R. Hoffmann, *Angew. Chem., Int. Ed.*, 2000, **39**, 2408–2448.
11 W. Schweika, R. P. Hermann, M. Prager, J. Persson and V. Keppens, *Phys. Rev. Lett.*, 2007, **99**, 125501.
12 E. Chalfin, H. Lu and R. Dieckmann, *Solid State Ionics*, 2007, **178**, 447–456.
13 V. Izard, M. Record and J. Tedenac, *J. Alloys Compd.*, 2002, **345**, 257–264.
14 M. Tsutsui, L. Zhang, K. Ito and A. Yamaguchi, *Intermetallics*, 2004, **12**, 809–813.
15 B. L. Pedersen, H. Birkedal, M. Nygren, P. T. Frederiksen and B. B. Iversen, *J. Appl. Phys.*, 2009, **105**, 013517.
16 J. Nylen, S. Lidin, M. Andersson, H. Liu, N. Newman and U. Haussermann, *J. Solid State Chem.*, 2007, **180**, 2603–2615.
17 B. L. Pedersen and B. B. Iversen, *Appl. Phys. Lett.*, 2008, **92**, 161907.
18 S. Ur, I. Kim and P. Nash, *Mater. Lett.*, 2004, **58**, 2132–2136.
19 S. Ur, P. Nash and H. Kim, *Mater. Lett.*, 2004, **58**, 2937–2941.
20 T. Caillat, A. Borshchevsky and J.-P. Fleurial, *Proc. Mater. Res. Soc.*, 1997, **478**, 103–108.
21 G. Nakamoto, N. Akai, M. Kurisu, I. H. Kim, S. C. Ur and V. L. Kuznetsov, *J. Alloys Compd.*, 2007, **432**, 116–121.
22 O. Prytz, A. E. Gunnaes, O. B. Karlsen, T. H. Breivik, E. S. Toberer, G. J. Snyder and J. Tafto, *Philos. Mag. Lett.*, 2009, **89**, 362–369.
23 B. L. Pedersen, H. Birkedal, E. Nishibori, A. Bentien, M. Sakata, M. Nygren, P. T. Frederiksen and B. B. Iversen, *Chem. Mater.*, 2007, **19**, 6304–6311.
24 F. Liu, X. Y. Qin and H. X. Xin, *J. Phys. D: Appl. Phys.*, 2007, **40**, 7811–7816.
25 A. P. Litvinchuk, J. Nylen, B. Lorenz, A. M. Guloy and U. Haeussermann, *J. Appl. Phys.*, 2008, **103**, 123524.

26 T. Ueda, C. Okamura and K. Hasezaki, *Mater. Trans.*, 2008, **49**, 2891–2894.
27 L. Zhang, M. Tsutsui, K. Ito and M. Yamaguchi, *J. Alloys Compd.*, 2003, **358**, 252–256.
28 B. Gault, E. A. Marquis, D. W. Saxey, G. M. Hughes, E. S. Toberer and G. J. Snyder, *Scr. Mater.*, 2010, **63**, 784–787.
29 S.-G. Kim, I. I. Mazin and D. J. Singh, *Phys. Rev. B: Condens. Matter Mater. Phys.*, 1998, **57**, 6199–6203.
30 T. Caillat, J.-P. Fleurial and A. Borshchevsky, *15th Int. Conf. Thermoelectrics*, 1996, 151–154.
31 H. J. Goldsmid and J. W. Sharp, *J. Electron. Mater.*, 1999, **28**, 869.
32 S. Bhattacharya, R. P. Hermann, V. Keppens, T. M. Tritt and G. J. Snyder, *Phys. Rev. B*, 2006, **74**.
33 Y. Wu, J. Nylen, C. Naseyowma, N. Newman, F. J. Garcia-Garcia and U. Haeussermann, *Chem. Mater.*, 2009, **21**, 151–155.
34 A. F. May; E. S. Toberer; A. Saramat; G. J. Snyder *Phys. Rev. B,* 2009, **80**, 125205.
35 E. S. Toberer, K. A. Sasaki, C. R. I. Chisholm, S. M. Haile, W. A. Goddard, III and G. J. Snyder, *Phys. Status Solidi RRL*, 2007, **1**, 253–255.
36 H. J. Kim, E. S. Bozin, S. M. Haile, G. J. Snyder and S. J. L. Billinge, *Phys. Rev. B*, 2007, **75**.
37 G. Nakamoto and M. Kurisu, *J. Electron. Mater.*, 2009, **38**, 916–919.
38 B. L. Pedersen, H. Birkedal, B. B. Iversen, M. Nygren and P. T. Frederiksen, *Appl. Phys. Lett.*, 2006, **89**, 242108.